PAPER

Check for updates

Carbon surface chemistry drives speciation and reactivity of cationic Fe species in CO_2 activation: a HERFD-XANES and valence-to-core XES study†

Matteo Aramini[a] and Rosa Arrigo (iD) *[ab]

While carbon-supported iron nanostructures are able to provide inexpensive frameworks where the dispersion of single-atom centres enables unique catalytic properties for carbon dioxide functionalization, detailed understanding of the structure of the transition metals is often prevented by the heterogeneous nature of the hosting C matrix and the variety of available sites, consequently hindering the understanding and development of CO_2 reduction chemistry. Herein, we report an experimental and computational spectroscopic investigation of few-layer graphene-based samples decorated with Fe atoms immobilised at the edges and in-plane defects of the graphene layers. We find that Fe–OH bound to N-terminated edge sites or in-plane defects of the graphene layers reacts with CO_2, forming bicarbonates. A similar reactivity is observed for Fe–OH bound to C-terminated edge sites, whereas Fe–OH coordinated to C-terminated in-plane defects remains unreactive towards CO_2. In stark contrast, FeN_4 sites in Fe–porphyrin present a direct, carbon-atom-mediated interaction with CO_2. These results provide insights into the local coordination environment of iron and its role in the reactivity towards CO_2 activation.

1. Introduction

In carbon-supported catalytic systems, the textural properties and surface chemistry of the carbon material play an essential role in determining the speciation, dispersion, and reactivity of metal species.[1–4] Functional groups and structural defects on these graphitic carbon supports — such as heteroatom-doped edges, vacancies — affect the electronic and geometric environments of anchored metals.[5–7] These characteristics enable fine control over metal–support interactions, which is crucial for tuning activity and selectivity in various reactions.[8,9]

Nitrogen-doped sites, especially those in substitutional forms, such as pyridine- and pyrrole-like configurations, are known to create localized charge accumulation/depletion on graphene edge sites that facilitate metal dispersion, stabilising single metal atoms or small clusters.[5] This stabilisation is often associated with enhanced catalytic performance, where specific dopant–metal interactions lead to improved turnover frequencies and durability compared to undoped carbons, as seen in electrocatalytic[10] as well as catalytic[11] oxygen reduction reaction and selective oxidation,[12,13] to name a few examples.

Additionally, the surface chemistry of the support dictates the proximity[8] and orientation of reactants to the active sites, as well modulating the adsorption energies of reaction intermediates.[14] For example, oxygen-containing groups, such as hydroxyl or carboxyl, can create a favorable microenvironment that aids in proton transfer or influences the hydration layer at the catalyst surface. Costentin *et al.*[15] found that modification of iron tetraphenyl porphyrin with phenolic groups considerably enhanced CO faradaic efficiency above 90% at low overpotential (0.465 V) and suggested that a high local concentration of protons associated with the phenolic hydroxyl substituents is the cause of such enhancement. Therefore, the microenvironment can alter the kinetics of key steps and thus the selectivity by creating stable active sites and regulating the access of reactants. This multifactorial effect of the carbon surface chemistry and its interplay with hosted catalytic centers are thus complex features to underpin, requiring predictive methods,[16,17] clarification of engineering aspects[18,19] and control of thermodynamic barriers for specific intermediates in CO_2 reduction.[20] In the liquid phase CO_2 reduction reaction (CO_2RR), Fe–N–C systems exhibit excellent faradaic efficiencies at very low overpotential,[21] especially for carbon–carbon (C–C) coupling reactions, which is particularly challenging to attain through CO_2 electroconversion.

Notwithstanding their appealing performances in CO_2RR at low overpotential, these materials exhibit poor stability at the lower potentials required for achieving operational

---

[a] *Diamond Light Source Ltd., Harwell Science & Innovation Campus, Didcot, Oxfordshire OX11 0DE, UK*

[b] *School of Science, Engineering and Environment, University of Salford, Manchester, M5 4WT, UK. E-mail: r.arrigo@salford.ac.uk*

5046 | *Catal. Sci. Technol.*, 2025, **15**, 5046–5054

This journal is © The Royal Society of Chemistry 2025

current densities, necessitating further development. Previous X-ray absorption near-edge structure (XANES) spectroscopy experiments identified a minority of Fe(II) species in Fe–N–C systems but could not clearly differentiate the coordination environment of Fe cations,[5,6,21] and therefore the precise nature of these species and their role in carbon dioxide chemisorption remain unclear. This study aims to elucidate the structure and electronic states of these Fe sites commonly found in N-doped carbon and determine their role in CO_2 activation, using synchrotron-based high-energy resolution fluorescence-detected X-ray absorption near-edge structure (HERFD-XANES) and valence-to-core X-ray emission spectroscopy (VtC-XES).

Compared to conventional XANES, HERFD-XANES significantly enhances the spectral resolution by avoiding the presence of 1 s core-hole lifetime broadening in the Fe K-edge absorption spectrum.[22] Combined with VtC-XES, which is highly sensitive to ligand environments, these techniques are best suited to unveil the nature of Fe–N sites and their distinction from Fe–O species as well as capture subtle electronic and ligand changes of the Fe species affected by the surface chemistry of the carbon support and the reaction in a CO_2 atmosphere.

To achieve this goal, we will investigate few-layer graphene-based samples decorated with Fe atoms immobilised at the edges and defects of graphene layers. We will compare the N-functionalised system (FeNG) with a sample obtained via Fe immobilisation on a few-layer graphene oxide (FeOG) and an Fe–porphyrin sample (FeTCPP).

We postulate that nitrogen defects in-plane and at the edge sites of the graphitic structure help localize π-conduction electrons, enabling the Fe-bound hydroxyl groups to react with CO_2 and form bicarbonate species. The high resolution of HERFD-XANES and the ligand sensitivity of VtC-XES enabled us to prove this hypothesis, providing insight and interpretation into the microscopic structures of Fe-N_4 sites responsible for the interaction with molecular CO_2.

2. Experimental

2.1. Preparation of FeNC and FeOC

The synthesis of the samples was previously reported.[5] Accordingly, 0.6 g of graphene oxide in powder form (796034-1G, Sigma-Aldrich, UK) was functionalized with ammonia (99.98% Ammonia Micrographic, BOC Linde) using a Carbolite MTF 10/25/130 furnace. The quartz tube, which held the sample in a ceramic boat, was purged with helium gas (BOC, 99.996%) at a flow rate of 50 mL min^{-1} for 30 min. Then, the gas flow was changed to ammonia (50 mL min^{-1}) and the sample was heated to 873 K at a temperature ramp rate of 10 K min^{-1} and held at this temperature for 4 h. Subsequently, the sample was cooled to 313 K in ammonia and further to room temperature in helium. The starting commercial few-layer graphene oxide and the ammonia-treated graphene oxide were used for Fe immobilisation via ion exchange, resulting in FeOG and FeNG, respectively. The

ion exchange was carried out using a 1 g L^{-1} aqueous solution of ferrous ammonium sulphate hexahydrate (99% Merck). 0.016 g of the graphene-based supports were suspended in 20 mL of the Fe-containing aqueous solution to which also 1 mL of pure ethanol was added. The suspension was left to exchange for 2 h at room temperature before being vacuum filtered and rinsed once with distilled water. The solid was dried in a vacuum oven at 383 K overnight then left in a desiccator at room temperature until used for characterization. Solid-state X-ray fluorescence (XRF) analysis of FeOG indicated an iron content of approximately 0.8% by weight. A sample of Fe-containing tetrakis(4-carboxyphenyl)porphyrin (Fe-TCPP) was prepared following a procedure reported in the literature:[23] a 250 mL, three-necked round-bottomed flask was charged with 0.50 g (0.635 mmol) of 4,4′,4″,4‴-(porphyrin-5,10,15,20-tetrayl)tetrabenzoic acid (TCPP) and N,N-dimethylformamide (80 mL). Upon complete dissolution of TCPP (via magnetic stirring), the solution was heated to reflux and iron(II) chloride tetrahydrate (1.54 g, 7.73 mmol) was added to the mixture. Refluxing was continued for 1 h while the temperature inside the flask was monitored with a thermocouple (ca. 428 K). After completion of the reaction, the solution was allowed to cool to below 373 K, at which point 6 M hydrochloric acid was added slowly and dropwise until all visible solid was dissolved. The mixture was cooled to room temperature and 100 mL of deionized water was added. The mixture was allowed to stand overnight and was then filtered under suction. Upon drying of the filter cake and washing with deionized water, a dark solid (0.41 g, 77%) was obtained. FeTCPP was characterized by UV-vis spectroscopy from a 10^{-5} M solution in tetrahydrofuran (THF). The solution was compared to meral-free TCPP. The absorption spectra of the metal-free porphyrins showed a typical Soret band at 420 nm and four Q bands with absorption maxima (515, 550, 590 and 650 nm). The UV-vis spectra of FeTCPP, shown in Fig. S1,† exhibited one Soret band and one Q band consistent with the literature, indicating the completion of the reaction.[24] XRF analysis of the solid-state sample indicated an iron content of approximately 16% by weight. The catalytic activity of the materials was tested via electroanalytical techniques, as illustrated in section 2.2 of the ESI.†

2.2. Characterization techniques

2.2.1. XAFS and XPS measurements. X-ray absorption experiments (XANES) were conducted at the I20 beamline of Diamond Light Source using a Si(111) four-bounce monochromator. Rhodium-coated harmonic rejection mirrors were used to remove high-energy harmonics and X-rays were focused horizontally and vertically via dedicated mirrors, achieving a beam size at sample position of ca. 400 μm (h) × 300 μm (w) (FWHM). The samples were either mixed with boron nitride, pelletized and measured in air or loaded in 3 mm Kapton capillaries and measured under in situ conditions within a plug-flow reactor. The absorption spectra were recorded in high energy resolution fluorescence

This journal is © The Royal Society of Chemistry 2025

Catal. Sci. Technol., 2025, 15, 5046–5054 | 5047

(HERFD) mode by means of an I20 XES spectrometer equipped with three Si(531) crystal analysers aligned at a Bragg angle of 73.09° on the Fe $K\beta_{1,3}$ emission line of a pure metal foil. An ion chamber filled to a 15% absorption was used for measurement of the incoming photons and XAS data were normalized using the Athena software with a linear pre-edge and polynomial post-edge background subtracted from the raw data. Fe $K\beta_{2,5}$ emission XES data were treated with the removal of a background, obtained *via* fitting the profile of Fe $K\beta_{1,3}$ emission spectra, and then normalized over the scattered intensity. The measurements were performed *ex situ* in air and *in situ* under flow conditions with samples enclosed in a tubular microreactor in Kapton fitted in a custom-made tube furnace built on the principles of the one reported earlier[25] and available on beamline I20 at the Diamond Light Source. *In situ* experiments were carried out under 15 mL min^{-1} He, followed by heating to 433 K in He. Subsequently the gas was switched to CO_2 15 mL min^{-1} at 433 K. XAS and XES spectra were recorded in different spots at each step. Temperatures were controlled *via* a K-type thermocouple.

X-ray photoelectron spectroscopy (XPS) measurements were performed at the B07 beamline of the Diamond Light Source synchrotron facility in the UK. A thin layer of the sample was drop-casted onto Au-coated silicon wafers. The XPS C 1s, N 1s and O 1s core levels were measured using an X-ray excitation energy corresponding to an electron kinetic energy (KE) of 450 eV. The pass energy (E_p) of the analyser was set to 20 eV. After each core level measurement, the Fermi edge was measured at the same excitation energy and used to calibrate the energy scale of the spectra. Samples were measured at room temperature and under UHV conditions as well as under a gas atmosphere introduced using a mass flow controller, and the pressure in the chamber was regulated *via* a butterfly valve. Heating was carried out using a button heater.[26]

2.2.2. Simulations. The XANES and VtC-XES spectra were simulated using a finite-difference method calculation code FDMNES.[27] The code solves the fully relativistic Schrödinger equation *via* the finite-difference method using density functional theory with a local exchange–correlation functional for the ground state. The final states used to compute the transition matrix elements are calculated on the excited electronic configuration by applying an energy-dependent exchange–correlation correction potential as in Hedin–Lundqvist. A spherical cluster centered on the scattering element was assumed, with a converged radius of 8 Å used for representing XANES and VtC spectra. Spectra have been convoluted with a core-hole lifetime broadening of 1 eV as implemented in the code. The investigated crystal structures were created by embedding Fe in-plane or at edge defects on a 25 Å wide fragment of graphene terminated with hydrogen atoms at the edges. Because of the large number of atoms and the uncertainty on the structures, the clusters were relaxed with classical molecular mechanics under the universal forcefield of the Forcite code within the Materials

Studio suite. More advanced settings including quadruple transitions, relativistic self-consistent field calculations and convolution methods were used in FDMNES for the generation of XAS/XES results, providing a more accurate reproduction of the experimental results.

3. Results and discussion

The Fe K-edge XANES spectrum of FeOG collected at room temperature shows pre-edge (1s → 3d transition) and edge (1s → 4p transition) resonances at *ca.* 7113.5–7115.5 eV and 7125 eV, respectively (Fig. 1). Such a spectrum is consistent with the XAS of Fe(III) species, as observed in Fe_2O_3 and ferrihydrite *Fh*-FeOOH (Fig. S2†).[21] The intensity and profile of the pre-edge suggest a predominant octahedral geometry. Upon thermal treatment in helium at 433 K (Fig. 1), the pre-edge changes to a single resonance at *ca.* 7114.4 eV. A more intense pre-edge at energy of ~7114 eV arises from the presence of some Fe species in coordination environments with a lower symmetry than octahedral sites, such as tetrahedral and distorted octahedral geometries.[27] At the same time, the intensity of the rising-edge transition at *ca.* 7123 eV increases and the intensity of the white line at 7132 eV decreases together with a broad feature at approximately 7137 eV gaining intensity. These spectral features are consistent with the coexistence of Fe(II) sites and Fe(III) sites.[21]

FeNG exhibits more intense ligand-field split pre-edge resonances (1s → 3d transition) compared to FeOG, suggesting more distorted Fe(III) octahedral sites (Fig. 1a). Moreover, a less intense white line and the presence of a shoulder at 7123 eV indicate the presence of Fe(II) sites already in the as-prepared sample. The presence of Fe(II) for impregnated Fe on N-functionalized C has also been observed on other types of C supports,[6] highlighting the possible role of the surface N species in the stabilization of these Fe(II) sites. The transformation observed upon thermal annealing of FeNG is similar in nature to those occurring in
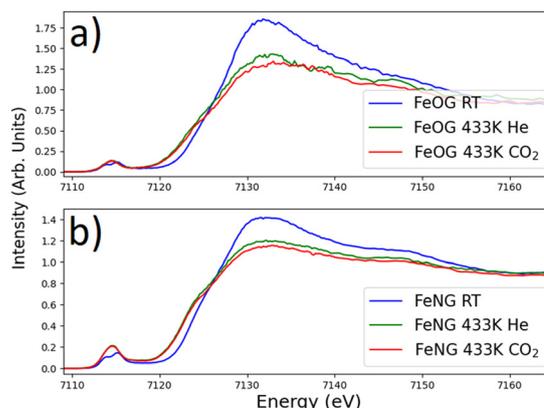

Fig. 1 (a) Fe K-edge XANES of FeOG measured at room temperature and in air (blue) and at 433 K and under a 15 mL min^{-1} CO_2 flow (red); (b) Fe K-edge XANES of FeNG measured at room temperature and in air (blue) and at 433 K and under a 15 mL min^{-1} CO_2 flow (red).

5048 | *Catal. Sci. Technol.*, 2025, **15**, 5046–5054

This journal is © The Royal Society of Chemistry 2025

FeOG but more pronounced (Fig. 1 and S3a†), suggesting a higher abundance of Fe(II) sites. Comparative analysis of FeOG and FeNG upon CO_2 chemisorption (Fig. 1 and S3a†) suggests that these sites should be involved in the chemisorption of CO_2. This can be seen from the difference spectrum in Fig. S3b,† generated by subtracting the spectrum measured under a CO_2 atmosphere from the spectrum under helium, showing positive contributions at approximately 7114, 7132 and 7144 eV, consistent with a change in the nature of the ligand causing a charge transfer from metal to ligand of the type Fe^{II}–L → Fe^{III}–L^-.[28] In contrast, the corresponding difference spectrum for FeOG (Fig. S3c†) shows negligible changes upon CO_2 adsorption. High-angle annular dark-field scanning transmission electron microscopy (HAADF-STEM) images for FeNG, shown in Fig. S4,† unveil the local coordination environment of Fe. We can identify a few isolated single Fe atoms occupying in-plane positions or decorating the edges of the graphene layers as well as agglomerated Fe atoms both on the basal planes and at the edge sites. Considering these topological characteristics, we model Fe-containing defects in the plane (Fe–N_4, Fe–O_4, Fe–C_4, Fe–$N_nC_{(4-n)}$, $FeO_nC_{(4-n)}$) and edges (Fe–N_2X, Fe–O_2X, Fe–C_2X, Fe–NCX, Fe–OCX, X = $(OH)_4$, $(OH)_3$) of a graphene layer, generate the corresponding XANES and valence-to-core profiles and perform a comparative experimental and theoretical analysis.

In order to explain the spectra of the samples at room temperature, we proceeded to compare the similarities between the experimental spectra and the ones simulated for an excess of 20 structures bearing diverse Fe coordination spheres and relaxed *via* computational methods. Simulated spectra are available in the ESI† (Fig. S5–S11). Based on such a screening and the linear combination fitting (LCF) of simulated spectra aiming to reproduce the relative intensities of the experimental XAS transitions, both FeOG and FeNG can be described with a combination of Fe present in two sites: Fe trapped at the edges of the graphene plane and Fe localised on in-plane defects. In the former, Fe at the graphene edges is coordinated with two atoms on an armchair termination of the plane. The choice of the armchair graphene termination is derived by TEM analysis (Fig. S4†). To reach an overall 6-fold coordination with O_h symmetry, the Fe atom binds additionally to four OH groups. In the latter defect, Fe occupies in-plane defects available when two sp^2 carbon atoms are removed to generate an in-plane di-vacancy on graphene oxide, providing a 4-fold coordination for Fe that is expanded in a pseudo O_h coordination *via* the addition of two apical OH groups. An example of such structures with N-terminations is graphically depicted in Fig. 2; analogous ones were generated for Fe sites bound to terminations with O, C and mixed ligand species. As shown in Fig. 3, the intensity of the experimental white lines suggests that the distribution of Fe in such defects is different between the two samples, and the LCF supports this conclusion. FeOG can be satisfactorily described with the combination of Fe
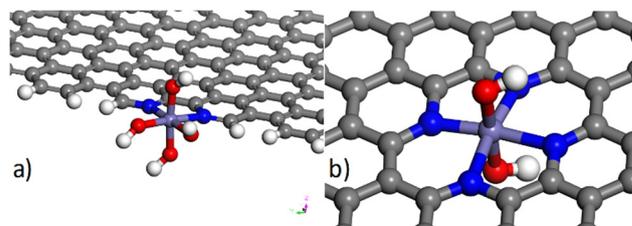

Fig. 2 Graphical representation of Fe single atom centres with hydroxyl ligands at the edge (a) and in-plane defects (b) of the graphene plane.

largely localised in Fe–$C_2(OH)_4$ defects (*ca.* 80–85%, shown as "edge-Fe(OH)$_4$ (2C)" in Fig. 3) and by in-plane ones with Fe bound to four C atoms on the plane and two axial OH (*ca.* 15–20% of the total, shown as "plane-Fe" in Fig. 3).

The lower white-line intensity of FeNG at 7130 eV is difficult to replicate with these two components only and forced us to consider a diverse environment for the edge Fe sites. XPS analysis indicates the existence of N species (Fig. S13†) in FeNG, in the form of pyridine-like N (binding energy (BE) ~398.5 eV) and metal-coordinated pyridine- or pyrrole-like nitrogen (BE ~400 eV).[21,29] Indeed, a good agreement with the HERFD-XAS results is reached only when considering Fe hosted within in-plane nitrogen inclusions and within edge Fe(OH)$_4$ units coordinated by nitrogen atoms that terminate the sp^2 sheet (Fig. 2). Indeed, results of linear combination fitting suggest that FeNG can be explained by considering Fe largely localised in Fe–$N_2(OH)_4$ defects (*ca.* 85%) and complemented by a minority fraction in in-plane ones (*ca.* 15% of the total), as shown by the results in Fig. 3. Based on the similarity amongst the simulated spectra using a combination of C, N and O atom terminations, we cannot exclude a more complex picture provided by an admixture of mixed graphene edge terminations, with C, N or O atoms, as considered in Fig. S8 and S9,† as well as a variety of C and N ligands in the 1st coordination sphere of
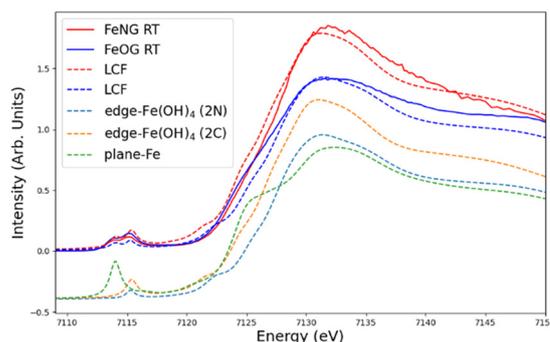

Fig. 3 Room temperature spectra of FeNG and FeOG in comparison with simulated spectra (dashed lines) for edge and in-plane Fe units. The defects labelled as "edge-Fe(OH)" correspond to Fe(OH)$_4$ units coordinated at the edge of a graphene plane on 2 N inclusions (model in Fig. 2a) and 2 C atoms belonging to an armchair termination of the graphene plane, which are indicated in parenthesis. LCF labels the best results of linear combination fitting of such defects, as described in the Results and discussion section. Atoms in parenthesis specify the in-plane atoms binding Fe in the simulated structures.

the in-plane Fe atom, as explored in Fig. S10 and S11 of the ESI.† The close resemblance of Fe K edge XANES profiles for Fe embedded in N_4 units and $N_nC_{(4-n)}$ coordination determines such a small change in the experimental data that prevents a quantitative structural identification.

When heating in the presence of CO_2, the spectra show a visible increase in intensity of the pre-edge, emergence of the feature at the rising edge at *ca.* 7124 eV and a general reduction of the intensity of the white-lines (Fig. S3†). The linear combination fitting of the XANES data of FeNG and FeOG in helium atmosphere at 433 K, shown in Fig. S12,† suggests that a redistribution of Fe atoms is achieved at high temperatures, with plane and edge Fe coexisting in similar proportion (*ca.* 50% each). Thus, the transformation observed in the XANES data can be attributed to changes in the number and nature of the ligands.

To help analyse such changes, we also collected $K\beta_{2,5}$ XES to take advantage of its sensitivity to light elements binding to iron. Fig. 4 and 5 show the $K\beta_{2,5}$ VtC emission spectra of FeOG and FeNG, respectively. Similarly for the two samples, the VtC spectra at room temperature show the $K\beta_{2,5}$ emission line centred at *ca.* 7107.5 eV, together with the $K\beta''$ feature around 7093 eV. A similar spectrum was reported for Fe–N–C systems obtained *via* ramp pyrolysis of Fe(II) acetate,10-phenanthroline and Zn(II) zeolitic imidazolate framework.[30] With the introduction of CO_2 at 433 K, the VtC spectrum of FeNG is slightly modified with an increase of scattered intensity on the high energy side of $K\beta_{2,5}$ around 7110 eV and a decrease on its low energy side around 7100 eV. Despite the lower signal-to-noise ratio, the same trend appears noticeable for the FeOG sample. The dashed lines in Fig. 4 and 5 show selected simulated XES spectra obtained from the model structures of Fe coordinated at the graphene edges and planes in its pristine form and after the inclusion of an axial bicarbonate ligand. Spectroscopic results from a wider range of geometries, where the coordination of CO_2
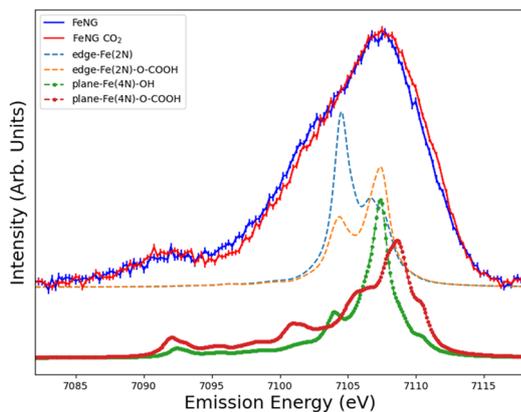

Fig. 5 $K\beta_{2,5}$ emission line of FeOG (continuous line) at RT and *in situ* under CO_2 flow at 433 K in comparison with simulated (dashed line) VtC emission spectra of selected structures of Fe single atom centres. Spectra have been applied a vertical offset for clarity. Atoms in parenthesis specify the in-plane atoms binding Fe in the simulated structures.
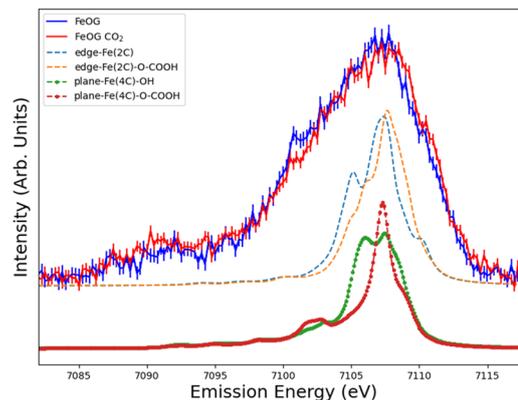
molecules and the covalent bonding to CO groups have been explored, are shown in the ESI† (Fig. S14). The XANES differences emerging with the coordination of CO_2 and CO on Fe would be inconsistent with the experimental data (Fig. S5 and S6†).

Hereafter, we propose an interpretation of the VtC spectra based on the geometry of the Fe defects, as derived from the HERFD-XANES analysis. This approach provides a unified interpretation of the results from both techniques and explains the incorporation of CO_2 into the structures as part of bicarbonate groups (Fig. 6 and 7). This finding is in agreement with the study of Zhang *et al.*, which investigated the effect of axial, O-coordinated FeN_4 units on the binding energy of intermediates in CO generation.[31] The coordination of CO_2-related species was confirmed by *in situ* C 1s and O 1s XPS data in Fig. S15.† The changes in the XES spectra indicate that FeNG has N coordinated (or mixed N/C) in-
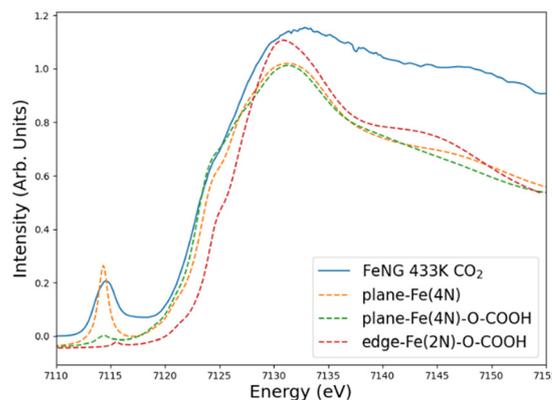

Fig. 4 $K\beta_{2,5}$ emission line of FeNG at RT and *in situ* during CO_2 flow at 433 K (continuous lines) in comparison with simulated (dashed line) VtC emission spectra of selected structures of Fe single atom centres. Spectra have been applied a vertical offset for clarity. Atoms in parenthesis specify the in-plane atoms binding Fe in the simulated structures.

Fig. 6 Comparison between the XANES absorption spectrum of FeNG in CO_2 flow at 433 K (continuous line) and simulated XAS spectra (dashed lines) for a selection of Fe single atom centres. Spectra have been applied a vertical offset for clarity. Atoms in parenthesis specify the in-plane atoms binding Fe in the simulated structures.

5050 | *Catal. Sci. Technol.*, 2025, **15**, 5046–5054

This journal is © The Royal Society of Chemistry 2025

Fig. 7 Comparison between the XANES absorption spectrum of FeOG in CO_2 flow at 433 K (continuous line) and simulated XAS spectra (dashed lines) for a selection of Fe single atom centres. Spectra have been applied a vertical offset for clarity. Atoms in parenthesis specify the in-plane atoms binding Fe in the simulated structures.
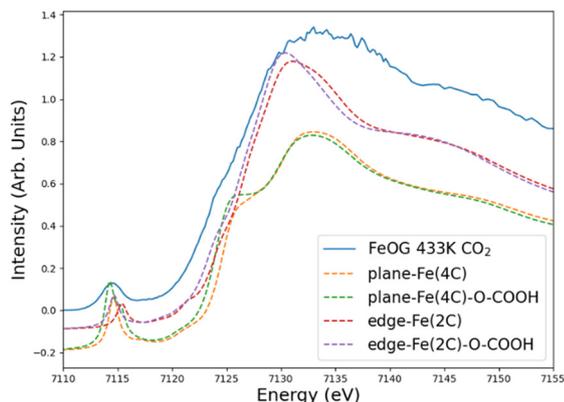
plane and edge Fe centres both trapping CO_2. This interpretation is confirmed in Fig. 6, where all the features are accurately reproduced in the XANES simulations. However, the change in the relative intensity of the pre-edge transitions *versus* edge intensity observed in the simulated spectra upon bicarbonate formation is abrupt, while it remains less pronounced in the experiments. Therefore, it can be inferred that only a fraction of the in-plane sites will accommodate CO_2 in the form of bicarbonate species. In contrast, FeOG spectral profiles can be reproduced considering C-coordinated Fe atoms at edges and in-plane sites, where only the former presents VtC changes in agreement with the experiment. Therefore, because of the relative shift of the centre of mass of the simulated VtC XES spectra, we postulate that in FeOG only edge-decorating Fe(III) species coordinate CO_2 in the form of bicarbonate species, within the experimental conditions explored herein. The XANES spectrum of FeOG (Fig. 7) confirms that in-plane defects are not likely to coordinate CO_2, as seen by the absence of a predicted doublet in the pre-edge region, indicative of an octahedral coordination, while the higher white-line intensity is consistent with CO_2 coordination at the edge defects. Additionally, the interpretation of these results together with the theoretical spectra of Fe-coordinated CO and CO_2 (Fig. S5–S8†) further suggests that direct interactions between Fe and CO or CO_2 are energetically unfavourable. Instead, these interactions are more likely mediated by out-of-plane O atoms as part of Fe-bound axial hydroxyl groups.[32]

In-plane Fe–N–C sites in graphene are often compared to molecular Fe–porphyrin systems. Therefore, we explored FeTCPP to identify the reactivity characteristics towards CO_2 for this type of Fe–macroligand species (Fig. S16a†) and compared it with the one of in-plane Fe atoms in graphene (Fig. S16b and S17†). The Fe K-edge XANES of FeTCPP in He at RT is characterised by a single pre-edge peak at 7114 eV, whereas the edge onset is 2 eV lower than that of FeNG and FeOG. The

component showing a peak at ~7114 eV arises from the mixture of Fe^{2+} and Fe^{3+}.[33] The XANES features at 7132 eV and 7140 eV emerge from Fe 4p states and are deeply influenced by the ligand nature and bond lengths. Upon adsorption of CO_2 at both RT and 433 K, an additional pre-edge feature appears at 7118 eV, which is attributed to a square planar D_{4h} symmetry of the metal centre.[34] This feature disappears if a coaxial ligand binds to Fe, resulting in a distortion of the square planar geometry towards a square pyramidal coordination of the Fe site. This is consistent with a displacement of the Cl^- ligand by CO_2 which is then weakly bound to the Fe site, leading to a square planar geometry.[34] A similar trend was observed for electrochemically prepared [Fe(II)TPP] complex under Ar and then CO_2.[35] The white line shows only minor changes upon CO_2 chemisorption at room temperature, indicating a relatively unchanged electronic structure, although the edge shifts slightly to lower energy. Upon heating to 433 K, a further shift of the edge is observed due to reduction while the resonance at 7132 eV decreases in intensity. It was suggested that a lower intensity of the 7132 eV peak with respect to the 7140 eV peak indicates a planar configuration of the Fe atom, whereas the opposite correlation is found when the Fe atom is in an out-of-plane configuration with respect to the macrocycle.[36] This, together with the increase of the 7118 eV resonance upon thermal treatment, would suggest that some CO_2-related species is indeed coordinated. However, the simulations in Fig. 6 and 7 show that the feature at 7118 eV appears when either CO or CO_2 is coordinated to the Fe–N_4 in in-plane sites *via* the C atom. In Fig. S16,† it is possible to see that such a feature is not clearly visible in FeNG and FeOG, consistent with a different reactivity of the graphene-derived samples towards CO_2. In analogy to the literature assignment,[36] the most intense resonance at 7132 eV in FeNG compared to the 7140 eV suggests that the Fe species assume an out-of-plane configuration. The VtC spectra of Fe TPPC show similar changes upon adsorption and annealing to FeNG and FeOG (Fig. S17†). The intensity of the peak at 7105 eV decreases and the peak at 7109 eV slightly shifts to higher energy. The intensity of the Kβ″ emission depends on the amount of metal np mixing into the ligand-centred, s-based molecular orbitals, where the energy of this feature is related to the ligand ionization potential.[37] The missing Kβ″ peak in the XES spectra of molecular Fe-TPPC at *ca.* 7092 eV is consistent with the absence of an Fe–O ligand.[30] In contrast, this peak is more pronounced for FeNG in CO_2, indicating an Fe–O ligand. The energy position of the $K\beta_{2,5}$ features depends on the nature of valence states and thus on the ligand (N *vs.* O). A shift to higher energy was found consistently when the coordination geometry increases due to the transformation from square planar to square pyramidal by the addition of a hydroxyl group, for example. The location within graphene seems also to affect the peak position, with different $K\beta_{2,5}$ profiles found for in-plane and edge Fe positions. This could be the results of different crystal field parameters originating from the constraints in the geometry experienced by Fe atoms. A high-energy shift upon CO_2 chemisorption indicates the emergence of ligand valence

states closer to the Fermi energy with p-character, potentially depending on a localization of the charge due to the electron-withdrawing effect of CO_2. We suggest that a 6-fold coordination environment of in-plane Fe sites in FeNG causes CO_2 to undergo nucleophilic attack from Fe-coordinated OH, leading to the formation of bicarbonate species. This interaction does not occur for in-plane defect sites in FeOG, which contains C-ligated Fe(III) atoms. It can be inferred that the higher charge accumulated on Fe sites due to N ligands increases the nucleophilic character of the axial hydroxyl group, which can react more promptly with CO_2. In the case of FeOG, N-rich in-plane sites are unlikely, leaving only hydroxyl groups bound to edge Fe sites with such a reactivity towards CO_2.

In contrast, our results suggest that CO_2 is adsorbed on Fe–N$_4$ sites of FeTCPP, leading to the formation of an Fe–C bond. This behaviour could be attributed to the different nature of the N ligand and the coordination environment in FeTCPP compared to FeNG, where geometric and electronic constraints govern its adsorption ability. In the FeTCPP system, the adsorption of CO or CO_2 modifies the central Fe atom into a site bearing lower point symmetry,[38] likely D_{4h} symmetry, by lifting the Fe atom out of the plane of the pyrrole nitrogen-containing macroligands. This structural distortion is consistent with an intermediate-spin Fe(II) site.[39] In contrast, Fe remains in a high-spin electronic state in the case of FeNG, as confirmed by the Fe K$\beta_{1,3}$ XES results shown in Fig. S18.† In this case, nitrogen adopts a pyridinic coordination environment (Fig. S13†), whereas the presence of pyrrolic nitrogen is difficult to discern due to the overlap in binding energy between this species and metal-cation-coordinated pyridinic nitrogen. We rationalise such a divergence with the availability of conduction electrons, provided by the graphene layer and exploited on Fe–C$_n$N$_{4-n}$ groups, to enable the formation of strong Fe–OH bonds which contribute to the binding of CO_2 molecules and determine the reactivity not observed in Fe–porphyrin molecules. It is important to note that these results pertain to thermal annealing at relatively low temperatures. However, it is possible that higher temperatures or the application of negative potentials during electrocatalysis, which are conditions compatible with the desorption of OH species, could also promote direct and dissociative CO_2 adsorption.

Some parallels can be drawn with the electroanalytical response of these systems, presented in Fig. S19–S23.† A more in-depth analysis of the results is included in the ESI.† Briefly, a CO_2-related Faraday process is observed for FeTCPP in the phase sensitive i–V curve of ac-V in CO_2-saturated sodium phosphate buffer solution, with an onset below −1 V vs. Ag/AgCl (Fig. S20d†). This Faraday charge transfer is attributed to the formation of a Fe(II)–CO_2^- species,[40] representing a direct reduction of CO_2.[41] This is consistent with the adsorption behaviour shown towards CO_2 in the in situ spectroscopic experiment presented here. At even lower potentials, charge is exchanged to a similar extent, regardless of the nature of the gas saturating the electrolyte solution, suggesting proton-coupled electron transfer.

In contrast, a low-level Faraday charge transfer is observed on FeOG by ac-V in the potential window from −1 to 0 V vs. Ag/AgCl (Fig. S21c†) in CO_2-saturated electrolyte. This result is consistent with a different mechanism of interaction with CO_2. Zhu et al.[42] observed that CO_2 adsorption on the catalyst surface began at potentials as low as 0.2 V vs. RHE (∼−0.4 V vs. Ag/AgCl at pH 7); however, the formation of the negatively charged CO_2^- intermediate was only detected at lower potentials, below −0.1 V vs. RHE. It must be noted that Faraday charge transfer in this large potential window might also arise from coupling with functional groups of graphene, amongst other reactions. The i–V profile in the ac-V measurements related to FeNG (Fig. S22c†) reveals a low-level faradaic current in a narrower window, between −0.8 V and −1.2 V vs. Ag/AgCl, and only under CO_2 saturation. We postulate that the current exchanged in this potential window is predominantly due to OH-mediated CO_2 adsorption on edge-located Fe(II)N$_4$–OH sites, which are found mostly irreversibly consumed in a second run. A small amount of direct CO_2 adsorption on the in-plane Fe(II)N$_4$–OH sites cannot be ruled out, as indicated by the presence of current exchange below −1 V vs. Ag/AgCl. This implies that the dominant species undergoing reduction on the graphene-based samples is HCO_3^-, which is initially formed via a surface chemical step facilitated by the availability of Fe-bound hydroxyl groups. In the subsequent step, once most of the hydroxyl groups are consumed, this chemical reaction can no longer proceed to the same extent as before. The low concentration of HCO_3^- in solution under the given experimental conditions results in low exchange currents within this potential window.

We attempt to correlate these results with literature findings on the performances of Fe–C systems in CO_2 electroreduction. The direct interaction of CO_2 with FeTCPP observed in our spectroscopic analysis is consistent with the mechanism proposed in the literature for Fe–phthalocyanine, which leads to CO formation.[40] N–C-supported cationic Fe species have been reported to produce formate and acetic acid at lower overpotential,[21] whereas CO is formed at much higher overpotential.[43,44] It can be postulated that a two-electron transfer mechanism occurs when hydroxyl species are involved in the CO_2 activation, leading to a reduction of adsorbed bicarbonate species into formate.

When hydroxyls are desorbed under a more negative voltage, direct coordination of CO_2 with Fe atoms can ultimately induce dissociation to CO,[43,44] followed by further reduction of CO to C–H$_x$ fragments.[8] However, at such low potentials, the cationic Fe species in graphitic C-supported Fe systems are transformed into metallic Fe, which is selective toward the hydrogen evolution reaction (HER),[21] making electroanalytical kinetic studies of CO_2 reduction difficult. Of particular interest is the ability of these N-containing systems to favour C–C coupling.[8,21] Our results suggest that heterogeneity in the electronic structure of the Fe sites in these FeNG systems along with their proximal location within the graphene layer creates an opportunity for C–C coupling. This may underlie the different electrocatalytic behaviour observed compared to FeTCPP.

5052 | Catal. Sci. Technol., 2025, **15**, 5046–5054

This journal is © The Royal Society of Chemistry 2025

The ability to produce organic products containing CH_x fragments appears to be related to the electron-donating effect exerted by the N ligands on Fe in in-plane positions. A HERFD XAS and non-resonant XES study attempted to explain the differing abilities of structurally homologous FeMoCo and FeVCo nitrogenases to reduce CO to short-chain hydrocarbons.[45] A more reduced state of Fe induced by V is suggested to enable a stronger CO binding via π backbonding, which, together with a less covalent Fe–V bond, facilitates the formation of short-chain hydrocarbon. A similar mechanism might be at play here.

4. Conclusions

We have presented an X-ray absorption and emission spectroscopic investigation aimed at clarifying the local geometry of iron sites in N-doped graphene material and their role in CO_2 activation.

We provide evidence of the presence of nitrogen in both in-plane defects and edge terminations hosting Fe atoms and reach the interpretation that N-doped sites are essential to explain the catalytic performances of the FeNG material, with both Fe decorating edges and Fe coordinated at in-plane defects of the N-doped graphene participating in the activation of CO_2.

In contrast to Fe molecular centers such as FeTPPC, where the interaction with CO_2 is thought to lead to the formation of Fe-CO bonds, we conclude that the interaction between N-doped Fe sites and CO_2 is mediated, under the explored conditions, by axial O atoms that provide electron density suitable for the nucleophilic attack responsible for the conversion of CO_2 into bicarbonate groups. Therefore, the in-plane Fe sites in FeNG systems differ significantly from the Fe–N_4 sites in FeTPPC, and together with the presence of Fe bound at the graphene edge-terminations and the possible heterogeneity of C and N ligands, explain the different reactivity of molecular systems containing Fe–N_4 sites and Fe-decorated graphene oxide systems. This study underscores the relevance of linking structural variations within inherently heterogeneous systems to distinct electronic structure signatures, demonstrating how subtle changes in coordination and local geometry are directly translatable into measurable spectroscopic and electrochemical responses.

Data availability

Data for this article are available at **https://salford-repository. worktribe.com**.

Author contributions

The authors contributed equally to this work.

Conflicts of interest

There are no conflicts to declare.

Notes and references

1 I. C. Gerber and P. Serp, *Chem. Rev.*, 2020, **120**(2), 1250–1349.
2 L. P. L. Gonçalves, J. P. S. Sousa, O. S. G. P. Soares, O. Bondarchuk, O. I. Lebedev, Y. V. Kolen'ko and M. F. R. Pereira, *Catal. Sci. Technol.*, 2020, **10**, 7217–7225.
3 T. Miah, P. Demoro, I. Nduka, F. De Luca, S. Abate and R. Arrigo, *ChemPhysChem*, 2023, **24**, e202200589.
4 F. De Luca, P. Demoro, I. Nduka, C. Italiano, S. Abate and R. Arrigo, *RSC Sustainability*, 2025, **3**, 1136–1148, DOI: **10.1039/ D4SU00463A**.
5 R. Arrigo, T. Sasaki, J. Callison, D. Gianolio and M. E. Schuster, *J. Energy Chem.*, 2022, **64**, 520–530.
6 R. Arrigo and M. E. Schuster, *Catalysts*, 2019, **9**, 303.
7 Y. Xie, D. Li, H. Dai and X. Chen, *Phys. Chem. Chem. Phys.*, 2025, **27**, 9211–9226.
8 R. Arrigo, R. Blume, V. Streibel, C. Genovese, A. Roldan, M. E. Schuster, C. Ampelli, S. Perathoner, J. J. Velasco Vélez, M. Hävecker, A. Knop-Gericke, R. Schlögl and G. Centi, *ACS Catal.*, 2022, **12**(1), 411–430.
9 R. G. Rao, R. Blume, M. T. Greiner, P. Liu, T. W. Hansen, K. S. Dreyer, D. D. Hibbitts and J.-P. Tessonnier, *ACS Catal.*, 2022, **12**(12), 7344–7356.
10 R. Arrigo, M. E. Schuster, Z. Xie, Y. Yi, G. Wowsnick, L. L. Sun, K. E. Hermann, M. Friedrich, P. Kast, M. Hävecker, A. Knop-Gericke and R. Schlögl, *ACS Catal.*, 2015, **5**(5), 2740–2753.
11 R. Arrigo, M. E. Schuster, S. Abate, G. Giorgianni, G. Centi, S. Perathoner, S. Wrabetz, V. Pfeifer, M. Antonietti and R. Schlögl, *ACS Catal.*, 2016, **6**(10), 6959–6966.
12 X. Li and Z. Xiang, *Nat. Commun.*, 2022, **13**, 57.
13 R. Arrigo, S. Wrabetz, M. E. Schuster, D. Wang, A. Villa, D. Rosenthal, F. Girsgdies, G. Weinberg, L. Prati, R. Schlögl and D. S. Su, *Phys. Chem. Chem. Phys.*, 2012, **14**(30), 10523–10532.
14 X. Li, S. Xi, L. Sun, S. Dou, Z. Huang, T. Su and X. Wang, *Adv. Sci.*, 2020, **7**, 2001545.
15 C. Costentin, S. Drouet, M. Robert and J.-M. Savéant, *Science*, 2012, **338**, 90–94.
16 J. Lei and T. Zhu, *ACS Catal.*, 2024, **14**, 3933–3942.
17 Y. Cai, X. Zhou, Y. Wang and Y. Li, *ACS Omega*, 2024, **9**(29), 32167–32174.

This journal is © The Royal Society of Chemistry 2025

Catal. Sci. Technol., 2025, **15**, 5046–5054 | **5053**

18 C. Liu, Y. Wu, K. Sun, J. Fang, A. Huang, Y. Pan, W. Cheong, Z. Zhuang, Z. Zhuang, Q. Yuan, H. L. Xin, C. Zhang, J. Zhang, H. Xiao, C. Chen and Y. Li, *Chem*, 2021, **7**, 1297–1307.

19 N. Mohd Adli, W. Shan, S. Hwang, W. Samarakoon, S. Karakalos, Y. Li, D. Cullen, D. Su, Z. Feng, G. Wang and G. Wu, *Angew. Chem.*, 2021, **60**, 1022–1032.

20 X. Li, S. Xi, L. Sun, S. Dou, Z. Huang, T. Su and X. Wang, *Adv. Sci.*, 2020, **7**, 2001545.

21 C. Genovese, M. E. Schuster, E. K. Gibson, D. Gianolio, V. Posligua, R. Grau-Crespo, G. Cibin, P. P. Wells, D. Garai, V. Solokha, S. Krick Calderon, J. J. Velasco-Velez, C. Ampelli, S. Perathoner, G. Held, G. Centi and R. Arrigo, *Nat. Commun.*, 2018, **9**(1), 935.

22 T. Lais, L. Lukashuk, L. van de Water, T. I. Hyde, M. Aramini and G. Sankar, *Phys. Chem. Chem. Phys.*, 2021, **23**, 5888–5896.

23 Y.-X. Jiang, T.-M. Su, Z.-Z. Qin and G. Huang, *RSC Adv.*, 2015, **5**, 24788.

24 W. Zheng, N. Shan, L. Yu and X. Wang, *Dyes Pigm.*, 2008, **77**(1), 153–157.

25 P. J. Chupas, K. W. Chapman, C. Kurtz, J. C. Hanson, P. L. Lee and C. P. Grey, *J. Appl. Crystallogr.*, 2008, **41**, 822–824.

26 D. C. Grinter, F. Venturini, P. Ferrer, M. A. van Spronsen, R. Arrigo, W. Quevedo Garzon and G. Held, The Versatile Soft X-Ray (VerSoX) Beamline at Diamond Light Source, *Synchrotron Radiat. News*, 2022, **35**(3), 39–47.

27 (*a*) Y. Joly, *Phys. Rev. B: Condens. Matter Mater. Phys.*, 2001, **63**, 125120; (*b*) M. L. Baker, M. W. Mara, J. J. Yan, K. O. Hodgson, B. Hedman and E. I. Solomon, *Coord. Chem. Rev.*, 2017, **345**(15), 182–208.

28 S. A. Wilson, E. Green, I. I. Mathews, M. Benfatto, K. O. Hodgson, B. Hedman and R. Sarangi, *Proc. Natl. Acad. Sci. U. S. A.*, 2013, **10**(41), 16333–16338, DOI: **10.1073/pnas.1315734110**.

29 R. Arrigo, M. Hävecker, S. Wrabetz, R. Blume, M. Lerch, J. McGregor, E. P. J. Parrott, J. A. Zeitler, L. F. Gladden, A. Knop-Gericke, R. Schlögl and D. S. Su, *J. Am. Chem. Soc.*, 2010, **132**(28), 9616–9630.

30 V. A. Saveleva, M. Retegan, K. Kumar, F. Maillard and P. Glatzel, *J. Mater. Chem. A*, 2023, **11**, 18862.

31 T. Zhang, X. Han, H. Liu, M. Biset-Peiró, J. Li, X. Zhang, P. Tang, B. Yang, L. Zheng, J. R. Morante and J. Arbiol, *Adv. Funct. Mater.*, 2022, **32**, 211144.

32 M. A. Velasco-Soto, S. A. Pérez-Garcia, J. Alvarez-Quintana, Y. Cao, L. Nyborg and L. Licea-Jiménez, *Carbon*, 2015, **93**, 967–973, DOI: **10.1016/j.carbon.2015.06.013**.

33 X. Sun, A. Tayal, A. Ullrich, O. Petracic and S. Haas, *J. Phys. Chem. C*, 2023, **127**(25), 12077–12083.

34 Q. Jia, N. Ramaswamy, H. Hafiz, U. Tylus, K. Strickland, G. Wu, B. Barbiellini, A. Bansil, E. F. Holby, P. Zelenay and S. Mukerjee, *ACS Nano*, 2015, **9**(12), 12496–12505.

35 D. Mendoza, S.-T. Dong, N. Kostopoulos, V. Pinty, O. Rivada-Wheelaghan, E. Anxolabéhère-Mallart, M. Robert and B. Lassalle-Kaiser, *ChemCatChem*, 2023, **15**(7), e202201298, DOI: **10.1002/cctc.202201298**.

36 X. Zhang, C. Chen, J. Dong, R.-X. Wang, Q. Wang, Z.-Y. Zhou and S.-G. Sun, *ChemElectroChem*, 2018, **24**(5), 3946–3952, DOI: **10.1002/celc.201801179**.

37 C. J. Pollock and S. DeBeer, *J. Am. Chem. Soc.*, 2011, **133**(14), 5594–5601.

38 A. Braun, L. B. Gee, M. W. Mara, E. A. Hill, T. Kroll, D. Nordlund, D. Sokaras, P. Glatzel, B. Hedman, K. O. Hodgson, A. S. Borovik, M. L. Baker and E. I. Solomon, *J. Am. Chem. Soc.*, 2023, **145**(34), 18977–18991.

39 C. Römelt, J. Song, M. Tarrago, J. A. Rees, M. van Gastel, T. Weyhermüller, S. DeBeer, E. Bill, F. Neese and S. Ye, *Inorg. Chem.*, 2017, **56**, 4745–4750.

40 N. Segura-Salas, R. Z. Snitkoff-Sol, D. Ragonis, S.-M. Kim, J. P. Hofmann, U. I. Kramm and L. Elbaz, Deconvoluting HER from CO2RR on an FeN4-Derived Catalyst Using Fourier-Transformed Alternating Current Voltammetry, *ACS Catal.*, 2025, **15**, 6266–6274.

41 Y. Zhang, L. Chen, F. Li, C. D. Easton, J. Li, A. M. Bond and J. Zhang, *ACS Catal.*, 2017, **7**(7), 4846–4853.

42 W. Zhu, S. Liu, K. Zhao, G. Ye, K. Huang and Z. He, *Small*, 2024, **20**, 2306144.

43 T. N. Huan, N. Ranjbar, G. Rousse, M. Sougrati, A. Zitolo, V. Mougel, F. Jaouen and M. Fontecave, *ACS Catal.*, 2017, **7**(3), 1520–1525.

44 A. S. Varela, M. Kroschel, N. D. Leonard, W. Ju, J. Steinberg, A. Bagger, J. Rossmeisl and P. Strasser, *ACS Energy Lett.*, 2018, **3**, 812–817.

45 J. A. Rees, R. Bjornsson, J. K. Kowalska, F. A. Lima, J. Schlesier, D. Sippel, T. Weyhermüller, O. Einsle, J. A. Kovacs and S. DeBeer, *Dalton Trans.*, 2017, **46**, 2445–2455.

46 G. Beckett, J. Beech-Brandt, K. Leach, Z. Payne, A. Simpson, L. Smith, A. Turner and A. Whiting, ARCHER2 Service Description, *Zenodo*, 2024, DOI: **10.5281/zenodo.14507040**.